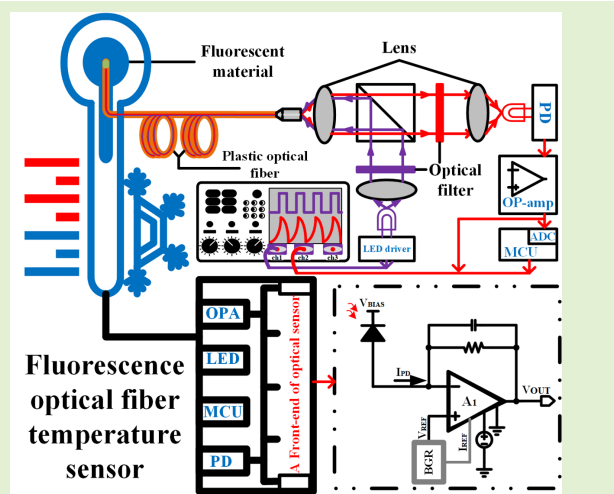


# An Integrated Fluorescence Optical Fiber Temperature Sensor Front-End Based on a Ring-Gate-Isolated Photodiode

Bingjun Xiong, Jian Yang, Yang Wang<sup>ID</sup>, Jian Guan, Feng Yan<sup>ID</sup>, Graduate Student Member, IEEE, Qian Zhang, Bhaskar Choubey<sup>ID</sup>, and Jingjing Liu<sup>ID</sup>

**Abstract**—Fluorescence optical fiber temperature sensors have found widespread use in harsh environments with electromagnetic interference, high voltages, flammability, and combustibility due to their excellent insulating properties. However, conventional fluorescence detection systems are constructed from discrete photodiodes and other front-end circuit chips, which cause bulky size, inferior detection efficiency, and degraded signal-to-noise performance. To address these issues, an integrated optical front-end circuit for fluorescence detection was proposed. The front-end circuit monolithically integrated a ring-gate-isolated photodiode (RGI-PD) device, a transimpedance amplifier (TIA), and a bandgap reference (BGR) circuit. The RGI-PD enabled the detection of the fluorescence afterglow signals, while the TIA circuit converted the photocurrent generated by the RGI-PD into a measurable photovoltage output. The RGI-PD utilized a P-well guard ring structure to prevent edge breakdown by isolating the avalanche region from the shallow trench. The dummy ring-gate created an inverted pyramid hole profile, focusing the electric field on the planar junction to enhance photodetection, which reduced trapping effects and dark counts. The proposed front-end circuit was fabricated using a standard 0.18  $\mu\text{m}$  bipolar CMOS DMOS (BCD) process. The measurement results demonstrated that the avalanche breakdown voltage (BV) of the RGI-PD was 13.05 V. The front-end circuit achieved a responsivity of 17.29 A/W at 500 nm wavelength, under a 13.88 V reverse bias voltage applied on the RGI-PD. Moreover, the front-end's dark voltage measured 0.908 V, with an optimal temperature coefficient (TC) of 41.01 ppm/ $^{\circ}\text{C}$  within the temperature range of  $-40^{\circ}\text{C}$  to  $85^{\circ}\text{C}$ . The proposed front-end circuit was suitable for fluorescence fiber temperature sensing applications.

**Index Terms**—Optical sensor, ring-gate-isolated photodiode (RGI-PD), transimpedance amplifier (TIA).



## I. INTRODUCTION

WITH the increasing demands for accurate temperature monitoring in industrial production, scientific research,

Manuscript received 18 January 2024; revised 11 February 2024; accepted 17 February 2024. Date of publication 28 February 2024; date of current version 16 April 2024. This work was supported by the National Natural Science Foundation of China under Grant 62174181 and Grant 62304007. The associate editor coordinating the review of this article and approving it for publication was Dr. Yongjia Li. (*Corresponding author: Jingjing Liu.*)

Bingjun Xiong, Jian Guan, Feng Yan, and Jingjing Liu are with the School of Electronics and Communication Engineering, Sun Yat-sen University, Shenzhen 518107, China (e-mail: xiongbj@mail2.sysu.edu.cn; liujj77@mail.sysu.edu.cn).

Jian Yang is with the School of Physics and Electronics, Hunan Normal University, Changsha 410081, China (e-mail: 514625349@qq.com).

Yang Wang is with the Key Laboratory of Microelectronic Devices and Circuits (MoE), School of Integrated Circuits, Peking University, Beijing 100091, China (e-mail: wangyangjyz@pku.edu.cn).

Qian Zhang is with School of Materials, Sun Yat-sen University, Shenzhen 518107, China (e-mail: zhangqian6@mail.sysu.edu.cn).

Bhaskar Choubey is with the Analogue Circuits and Image Sensors, Siegen University, 57076 Siegen, Germany (e-mail: bhaskar.choubey@uni-siegen.de).

Digital Object Identifier 10.1109/JSEN.2024.3369050

and medical fields, traditional temperature sensors using active electrical signals are revealing limitations [1], [2]. In microwave cancer treatment in the medical field, the accurate control of hyperthermia temperatures directly affects the treatment outcomes. In power systems, poor contact between cable joints and breakers can easily generate hot spots and cause fires under high currents, therefore real-time monitoring of contact point temperatures is also needed. Traditional thermocouples and thermistors using electrical signals as transmission media are susceptible to electromagnetic interference leading to decreased accuracy. They also pose safety hazards in high-voltage environments. In contrast, fluorescent optical fiber temperature sensors using optical signals as transmission media can effectively resist external electromagnetic interference and are well-suited for harsh environments with strong electromagnetism, high pressure, flammability, and explosiveness [3]. With the increasing demand for accurate temperature monitoring, fluorescent optical fiber temperature sensing technology has shown significant application prospects and development

potential in industrial, medical, and other fields, attributable to its outstanding insulation performance and anti-interference capabilities [4]. However, fluorescence detection systems constructed from discrete components have drawbacks like large volume, low detection efficiency, complex hardware circuits, and low signal-to-noise ratios (SNRs) [5]. Therefore, research into integrated photoelectric conversion circuits on a single chip is helpful in overcoming the limitations of traditional discrete systems and achieving optimal signal-matching paths, thereby greatly improving the detection accuracy of the system.

An essential component for such systems would be a photodiode. Photodiodes manufactured by standard CMOS process have been widely utilized in fluorescence detection, with their photoelectric conversion properties crucially impacting the accuracy of the detection system [6], [7], [8]. The fluorescent fiber optic temperature sensor measures temperature by detecting the fluorescence emission from rare earth materials, which are excited by a light source. Once the excitation stops, the fluorescence decays exponentially with a temperature-dependent fluorescence lifetime. This lifetime is quantified to achieve accurate temperature measurement [9], [10], [11]. Photodiodes and other optoelectronic devices can detect and convert such fluorescent signals into photocurrents. Typically, a transimpedance amplifier (TIA) circuit is then used to convert these photocurrents into photovoltages for further processing and digitization [12], [13], [14], [15]. Accurate fluorescence lifetime can be obtained by processing these photovoltage signals, achieving precise temperature values. The integration of photodiode and TIA circuits on a single chip eliminates the common problems in discrete designs, such as leakage current errors, noise pickup, and gain peaking due to stray capacitance. Significant improvement in system SNR and reduction of system size has been achieved in similar other systems [16], [17]. Investigating photoelectric TIA circuits with full on-chip integration of photodiodes, hence, can be beneficial for improving the detection accuracy of optical sensor systems.

A number of studies have reported the integration of optoelectronic devices and peripheral circuits for fluorescence detection [18], [19], [20]. Rae et al. [21] developed a CMOS-based microsystem specifically designed for time-resolved fluorescence measurements. Their dual-chip microsystem based on a  $0.35\text{ }\mu\text{m}$  CMOS process, integrates excitation, detection, and filtration, achieving a compact fluorescence lifetime analysis system by bump-bonding the driver array to the light-emitting diodes (LED) [21]. Substantial further research has also been undertaken to obtain a higher degree of integration of photodiodes and signal-processing circuits. Bronzi et al. [22] demonstrated a  $64 \times 32$  single-photon avalanche diode (SPAD) array sensor utilizing a high-voltage  $0.35\text{ }\mu\text{m}$  CMOS process. The sensor is able to process 2-D or 3-D information at the pixel level, thereby having fluorescence lifetime imaging and laser radar 3-D ranging functionalities [22]. Manickam et al. [23] proposed a CMOS biosensor chip for continuous wave fluorescence detection. The chip utilizes photodiodes as optical sensors and a sigma-delta modulator-based photodetector to successfully detect human respiratory viruses [23]. This demonstrates

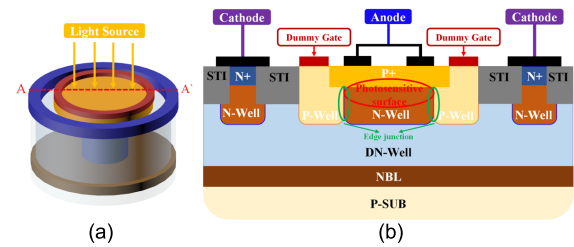


Fig. 1. (a) Three-dimensional structure of the RGI-PD device. (b) Two-dimensional cross-sectional view of the RGI-PD device.

the potential of CMOS-based optical sensors for biomedical applications. Hong et al. [24] realized a fully integrated fluorescence-based biomolecular sensor based on a  $65\text{ nm}$  CMOS process. Their biosensor integrates a photodetection circuit, a capacitively coupled TIA, a correlated double sampling circuit, and a filter based on nano-plasmonic waveguides, achieving over  $50\text{ dB}$  suppression ratio over a wide range of incident angles [24]. Choi et al. [25] developed an implantable 3-D deep brain fluorescence imager using a  $0.13\text{ }\mu\text{m}$  BCD process [25]. As a result, photodiodes in the CMOS process can be a promising candidate for fluorescence measurement. These studies also demonstrate the promise of full integration of optoelectronic devices and signal processing circuits in effectively reducing system cost, size, and complexity. However, the photodiodes in these studies all suffered from high avalanche breakdown voltage (BV) and low responsivity. These drawbacks significantly limit the integration of the photodiode with subsequent signal-processing circuits. Furthermore, the high BV also increases the power dissipation of these systems. This article aims to solve these problems by proposing a photodiode with low avalanche BV and high responsivity. It further integrates an optical front-end, an optical front-end sensor circuit integrating detection and amplification functionalities was designed and implemented.

In this article, an integrated front-end circuit of a fluorescence optical temperature sensor consisting of a ring-gate-isolated photodiode (RGI-PD) device and a TIA with a bandgap reference (BGR) is proposed. We believe this is the first temperature measurement application of these diodes, which shows promising results and potential for further integration. The rest of this article is organized as follows. Section II introduces the structure and principle of the proposed RGI-PD device. Section III introduces the proposed front-end circuit. The experimental results and discussions are presented in Section IV. Section V concludes this article.

## II. STRUCTURE AND PRINCIPLE OF THE RGI-PD DEVICE

Fig. 1(a) shows the proposed RGI-PD's 3-D structure, whereas Fig. 1(b) depicts its cross section view. This device in a circular shape, combines a highly doped P+ region and a lightly doped N-Well to establish the photosensitive surface. The N+ region acts as the cathode with a high potential, and the P+ region functions as the anode with a low potential, creating a vital voltage gradient within the device. When the potential of N+ reaches the reverse BV of P+/N-Well, a strong electric field force is generated on the photosensitive surface, leading to the formation of an avalanche multiplication

region. When a fluorescence photon reaches the avalanche multiplication region, it induces electron excitation in the valence band, resulting in the generation of electron-hole pairs. Subsequently, the avalanche multiplication effect leads to an exponential increase in the number of photogenerated carriers, resulting in a significant amplification of the anode current.

The proposed RGI-PD device was designed and fabricated using a  $0.18\text{ }\mu\text{m}$  BCD process. Inspired by the photodiode design in [18], the proposed RGI-PD utilizes a P-Well with dummy gate isolation rings as virtual guard rings, preventing edge breakdown in the avalanche multiplication region. Separating the avalanche multiplication region from the shallow trench isolation (STI) avoids carrier trapping at defect states, reducing dark current and noise. At the same time, the RGI-PD device has a virtual guard ring with an inverted pyramid-shaped local hole concentration characteristic, which improves the responsivity of the device and further enhances the photodetection efficiency of the photodiode. When this RGI-PD device is under reverse bias, i.e., the N-type doped region is at a higher potential and the P-type doped region is at a lower potential, the dummy ring gate can form a vertical upward driving electric field. Thus, the holes in the P-Well are attracted to the surface of the dummy ring gate, enhancing the local hole concentration on the P-Well surface and achieving the goal of strengthening the virtual guard ring. Moreover, as the local hole concentration decreases in an inverted pyramid shape downward from the virtual P-Well guard ring, the electric field of the avalanche multiplication region can be focused on the planar photosensitive p-n junction. This reduces the electric field intensity at the edge of the multiplication region. This structure can not only effectively suppress the deep level trapping effect caused by material defects to reduce dark count rate, but also improve the responsivity and photodetection efficiency of the photodiode device. Furthermore, the design principles of photoelectric p-i-n diodes are applied to create the cathode N-type region, which consists of N-Well, Deep N-Well (DN-Well), and N-type Buried Layer (NBL). These layers can enhance charge collection in the multiplication region and broaden the spectral response range of the RGI-PD device. Additionally, the NBL forms a reverse p-n junction with the P-SUB and effectively mitigates the influence of substrate noise carriers on the device.

The RGI-PD structure was simulated. In the simulations, a  $14\text{ V}$  bias voltage was applied on the cathode with the anode grounded. Fig. 2 presents the electric field and impact ionization distributions under normal operation. Likewise, the distribution curves of the transverse electric field and transverse impact ionization are shown in Fig. 3. One may observe that the electric field is concentrated primarily at the planar p-n junction of the device, while the peak intensity of impact ionization is predominantly centered in the middle of the planar junction. The electric field intensity of the planar p-n junction formed by the P+/N-Well is approximately  $5.82 \times 10^5\text{ V/cm}$ , while the same at edge is  $4.36 \times 10^5\text{ V/cm}$ . This confirms that the dummy ring gate isolation P-Well guard ring is effective in preventing edge breakdown. Furthermore, a weak electric field intensity is present beneath the dummy ring gate of the RGI-PD device, indicating that the dummy

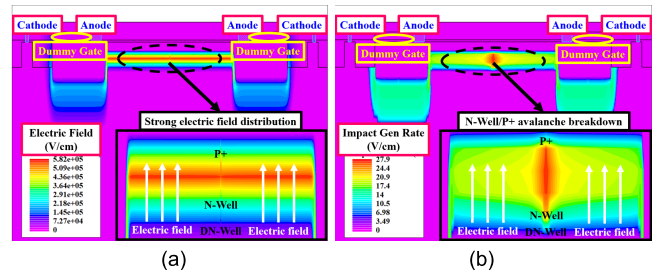


Fig. 2. Electric field distribution and the impact ionization distribution of RGI-PD device. (a) Electric field distribution. (b) Impact ionization distribution.

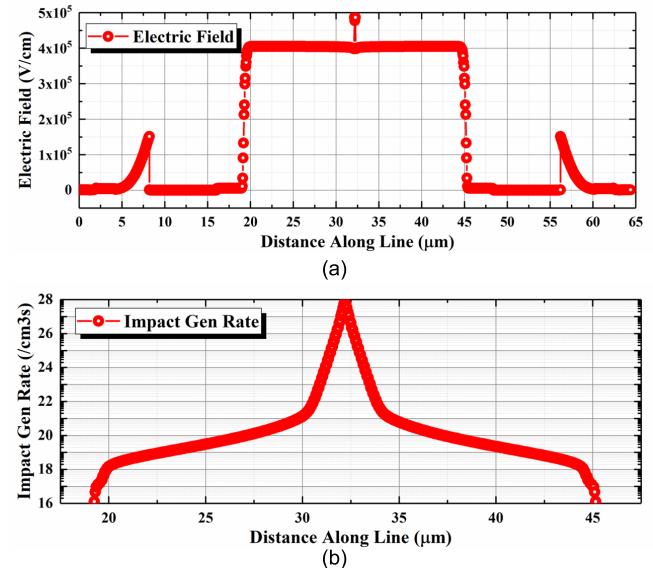


Fig. 3. Transverse distribution of RGI-PD device. (a) Electric field distribution. (b) Impact ionization distribution.

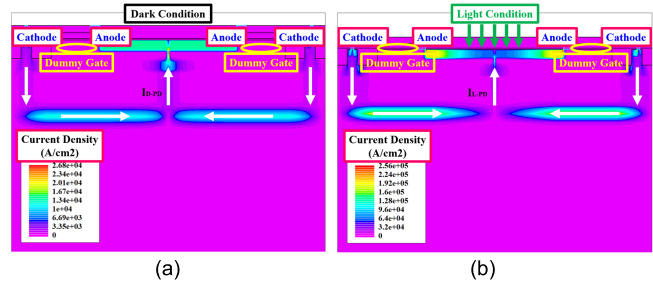


Fig. 4. Dark current density and light current density of RGI-PD device. (a) Dark current density. (b) Light current density.

ring gate isolation structure can influence the local hole concentration of the P-Well guard ring and thus affect the device characteristics. As intended in our design, the dummy ring gate forms a vertically upward electric field. The existence of this electric field results in an inverted pyramid-shaped hole concentration in the P-Well, thereby enabling the electric field of the avalanche multiplication region to be focused on the planar photosensitive p-n junction, so as to improve the responsivity and detection efficiency of the device. Table I presents the simulated concentration and significant size information of the RGI-PD device.

The total current density distributions of the RGI-PD device under dark and light conditions are shown in Fig. 4. Under a strong electric field, dark carriers initiating an avalanche effect at the photosensitive surface result in the RGI-PD device's

**TABLE I**  
SIMULATED CONCENTRATION AND SIGNIFICANT SIZE INFORMATION OF THE RGI-PD DEVICE

Device name	RGI-PD
Active area P+	32 $\mu\text{m}$
Active area N+	2.2 $\mu\text{m}$
Dummy ring-gate isolation	8 $\mu\text{m}$
P+/N+ (TCAD)	$1 \times 10^{20} \text{ cm}^{-3}$
P-Well/N-Well (TCAD)	$1.5 \times 10^{17} \text{ cm}^{-3}$
DN-Well (TCAD)	$1 \times 10^{16} \text{ cm}^{-3}$
NBL (TCAD)	$1 \times 10^{20} \text{ cm}^{-3}$

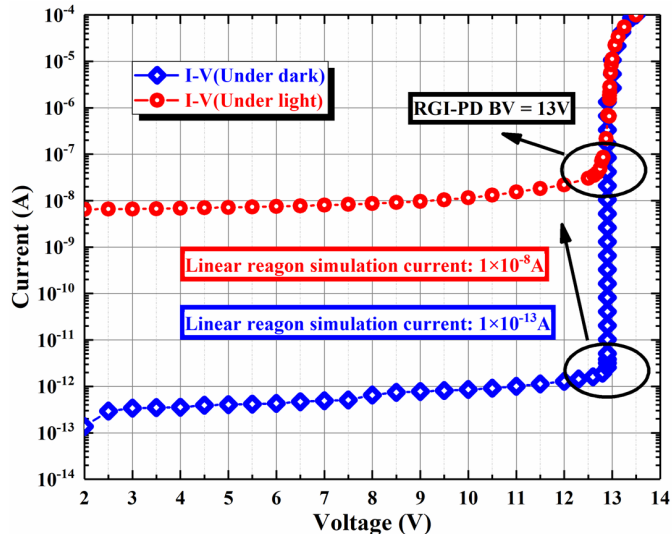


**Fig. 5.** Simulated the current-voltage characteristics of the RGI-PD device.

current primarily concentrating in the NBL region. The high doping concentration in the NBL reduces on-resistance, thus enabling a current loop from the cathode N+ to the anode P+. Consequently, this generates a dark current density of  $2.68 \times 10^4 \text{ A/cm}^2$ . Similarly, when photons strike the photosensitive surface and trigger an avalanche effect, the current pathway in the RGI-PD remains unchanged. However, the photocurrent density significantly increased to  $2.56 \times 10^5 \text{ A/cm}^2$ . Fig. 5 depicts the simulated current–voltage (*I*–*V*) characteristics of the RGI-PD device, and the reverse bias voltage was varied from 0 to 14 V. It can be observed that the RGI-PD device exhibits a BV of 13 V. The simulation results reveal that the RGI-PD’s output dark current (depicted by the blue line) remains constant at  $1 \times 10^{-13} \text{ A}$  within the linear region. Under illuminations (550 nm wavelength and 2 W/ $\mu\text{m}^2$  optical power), the device’s output current (indicated by the red line) is  $1 \times 10^{-8} \text{ A}$  in the linear region, confirming the photodetection mechanism. When the voltage across the RGI-PD reaches the avalanche BV (13 V), the avalanche effect caused by photons or noise carriers occurs and the device reaches a saturation state (in the order of  $\mu\text{A}$  or mA). The simulation results of the *I*–*V* characteristics also show that the RGI-PD device exhibits outstanding avalanche multiplication effects, which satisfy the requirements for fluorescence detection. The spectral response of the RGI-PD device was also simulated by vertically illuminating its photosensitive region with varying light wavelengths (100 to 1200 nm) at an optical power density of 2 W/ $\mu\text{m}^2$ . Fig. 6 shows the spectral responses under three

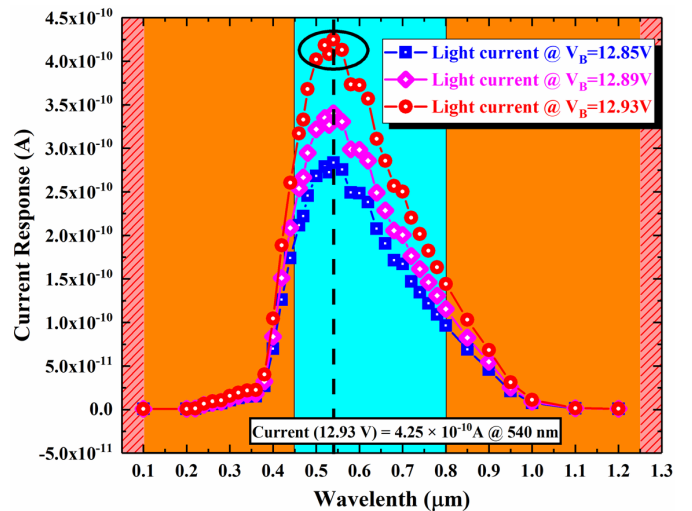


**Fig. 6.** Simulated the spectral response characteristics of the RGI-PD device.

different bias conditions. The stimulated photocurrents were recorded at the reverse bias voltages of 12.85, 12.89, and 12.93 V to construct the device’s spectral response curves. It can be observed that the photosensitive PN region, consisting of the P+ region and the N-type depleted region (including N-Well, DN-Well, and NBL), has a spectral response range of 450 to 800 nm. The response peak is at 540 nm, and the excitation light current value is  $4.25 \times 10^{-10} \text{ A}$ , which would be expected from typical silicon-based devices. Furthermore, the photoelectric current response of the device increased with an increase in bias voltage. The photocurrent produced by these diodes needs to be buffered and converted into a voltage for further processing and digitization. To do so, we use further signal conditioning circuits explained in the next section.

### III. DESIGN OF THE FRONT-END CIRCUIT WITH RGI-PD

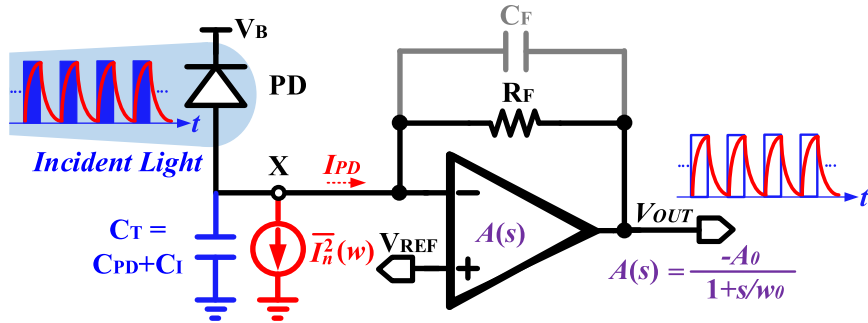
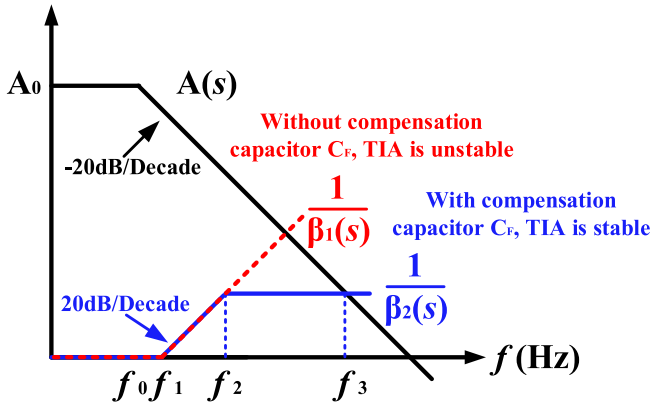
The TIA serves as a critical front-end amplifier for fluorescence optical temperature sensors. Its primary function is to convert weak optical signals into electrical signals and amplify them to a desired level, thereby enabling proper signal processing in optical sensor systems. A simplified schematic of TIA is shown in Fig. 7. It consists of a feedforward amplifier  $A(s)$  and a feedback resistor  $R_F$ , which converts the photocurrent  $I_{PD}$  generated from the PD into an output voltage  $V_{OUT}$ .  $C_T$  is the total capacitance at the TIA input node, including the parasitic capacitances of  $C_{PD}$ , and the TIA input  $C_I$ . Considering the case without the compensation capacitor  $C_F$ , the TIA can be modeled as a second-order system assuming the feedforward amplifier  $A(s)$  has a single dominant pole  $\omega_0$  and a passband voltage gain  $A_0$ . Therefore, the passband transimpedance gain of the TIA is given by

$$R_T = R_F \cdot \frac{A_0}{1 + A_0} \approx R_F. \quad (1)$$

The TIA bandwidth ( $BW_{3\text{dB}}$ ) can be expressed as follows:

$$BW_{3\text{dB}} = \frac{\sqrt{2A_0(1 + A_0)}}{2\pi R_F C_T} \approx \frac{\sqrt{2}A_0}{2\pi R_F C_T}. \quad (2)$$

The total TIA input-referred noise (IRN) current power spectral density is the sum of the IRN current power spectral

Fig. 7. Configuration of a typical TIA with compensation capacitor  $C_F$ .Fig. 8. Frequency response characteristics of TIA with (without) compensation capacitor  $C_F$ . The black, red, and blue traces represent the frequency responses of  $A(s)$ ,  $1/\beta_1(s)$ , and  $1/\beta_2(s)$ , respectively.

density of the feedback resistor and the feed-forward amplifier. It can be expressed as follows:

$$\overline{I_n^2(f)} \approx \frac{4kT}{R_F} + 4kT\gamma \frac{(2\pi C_T)^2}{g_m} f^2 \quad (3)$$

where  $g_m$  is the total transconductance of the input stage of the feedforward amplifier,  $T$  is the absolute temperature,  $k$  is Boltzmann's constant, and  $\gamma$  is the transistor excess noise factor.

The stability of a TIA is crucial for ensuring consistent functionality and reliable performance. The TIA's feedback network comprises a single-pole  $RC$  filter with the feedback resistance  $R_F$  and the total input capacitance  $C_T$ . The feedback coefficient of the TIA can be expressed as

$$\beta_1(s) = \frac{1/sC_T}{R_F + 1/sC_T} = \frac{1}{1 + s \cdot R_F C_T}. \quad (4)$$

The reciprocal of the feedback coefficient can be calculated using (4) as

$$\frac{1}{\beta_1(s)} = 1 + s \cdot R_F C_T. \quad (5)$$

The compensation capacitor  $C_F$  is connected in parallel with the feedback resistor to provide necessary compensation and ensure a sufficient phase margin. By incorporating the compensating capacitor  $C_F$ , the feedback coefficient of the TIA can be expressed as

$$\beta_2(s) = \frac{1/sC_T}{R_F/(1/sC_F + 1/sC_T)} = \frac{1 + s \cdot R_F C_F}{1 + s \cdot R_F (C_T + C_F)}. \quad (6)$$

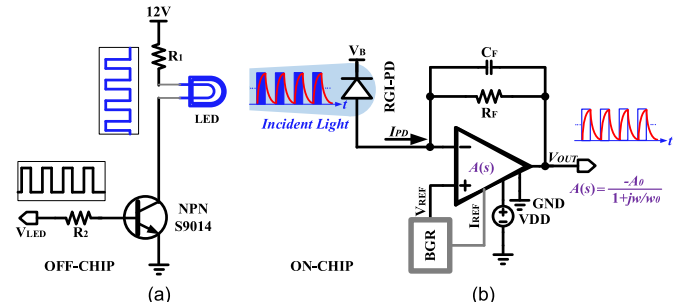


Fig. 9. (a) Schematic of the off-chip LED driver circuit. (b) Proposed on-chip optical sensor front-end circuit.

Fig. 8 depicts the frequency response of  $A(s)$ ,  $1/\beta_1(s)$ , and  $1/\beta_2(s)$ .  $A(s)$  maintains a stable gain  $A_0$  at low frequencies and decreases with 20 dB/dec after the dominant pole at  $f_0$ . Likewise,  $1/\beta_1(s)$  is a uniform gain of one at the low-frequency band and starts to increase after  $f_1$  with 20 dB/dec. The intersection point of the  $A(s)$  and  $1/\beta_1(s)$  curves represents the frequency of  $A_0\beta_1(s) = 1$ , which determines the phase margin. The convergence rate of  $A(s)$  and  $1/\beta_1(s)$  curves is 40 dB near the intersection point, indicating a potential circuit instability [26]. Comparison of (4) and (6) reveals that incorporating the compensating capacitor  $C_F$  not only adjusts the dominant pole of the loop gain, but also introduces an additional zero. This zero counteracts the phase shift caused by the dominant pole and alters the convergence rate of  $A(s)$  and  $1/\beta_2(s)$  to 20 dB. As a result, the phase margin of the TIA circuit is increased, which improves its stability.

The designed front-end circuit diagram of the optical sensor is shown in Fig. 9(b). It consists of the proposed RGI-PD, a feedforward amplifier  $A(s)$ , a BGR circuit, a feedback resistor  $R_F$ , and an on-chip compensating capacitor  $C_F$ . The RGI-PD operates under a reverse bias voltage  $V_B$  and exhibits a linear relationship between its output current and light intensity. The compensation capacitance  $C_F$  is generally much larger than the sum of the photodiode junction capacitance and the amplifier's input equivalent capacitance. The transfer function of this front-end circuit can be modeled by the following first-order expression

$$V_{OUT} = V_{REF} - I_{PD} \cdot R_F. \quad (7)$$

Recollecting the working principle of the fluorescent optical fiber temperature sensor, when the excitation light source is turned off, the fluorescent signal is known to decay

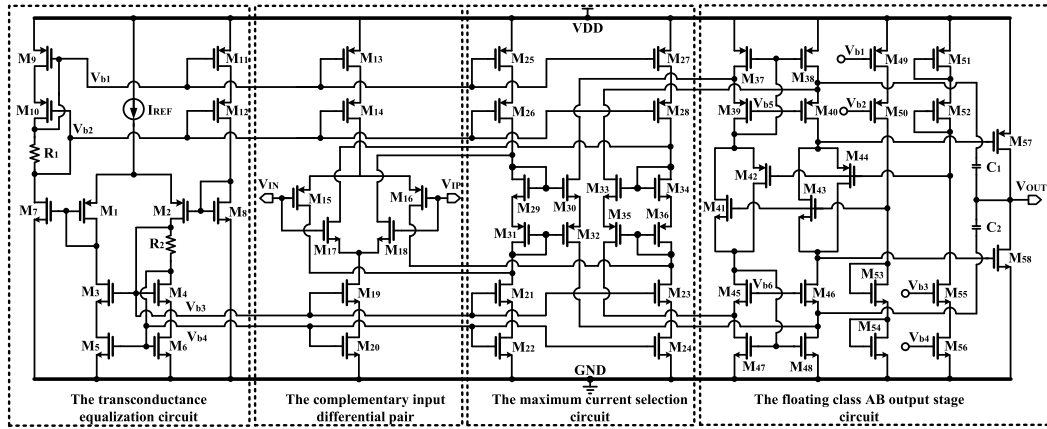


Fig. 10. Circuit diagram of the feedforward amplifier.

TABLE II  
DESIGN PARAMETERS AND KEY SIZE INFORMATION  
OF FEEDFORWARD AMPLIFIER

Transistor	W/L×M	Transistor	W/L×M	Device	Parameter
M <sub>1</sub>	12/2×4	M <sub>30</sub>	8/2×4	M <sub>43</sub>	10/2×1
M <sub>2</sub>	12/2×4	M <sub>31</sub>	16/2×4	M <sub>44</sub>	20/2×2
M <sub>7</sub>	8.5/4×2	M <sub>32</sub>	16/2×4	M <sub>51</sub>	16/2×2
M <sub>8</sub>	8.5/4×2	M <sub>33</sub>	8/2×4	M <sub>52</sub>	36/2×2
M <sub>15</sub>	30/4×2	M <sub>34</sub>	8/2×4	M <sub>53</sub>	8/2×1
M <sub>16</sub>	30/4×2	M <sub>35</sub>	16/2×4	M <sub>54</sub>	12/2×1
M <sub>17</sub>	10/4×2	M <sub>36</sub>	16/2×4	M <sub>57</sub>	20/2×4
M <sub>18</sub>	10/4×2	M <sub>41</sub>	10/2×2	M <sub>58</sub>	10/2×4
M <sub>29</sub>	8/2×4	M <sub>42</sub>	60/2×2	C <sub>1</sub> =C <sub>2</sub>	10/10×15

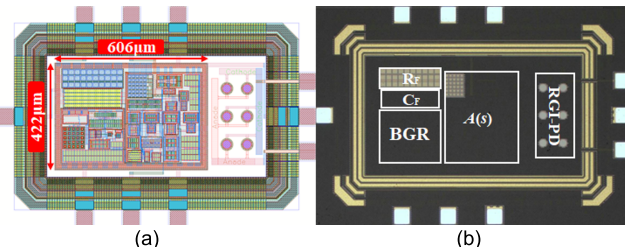


Fig. 11. (a) Layout of the proposed optical sensor front-end circuit. (b) Micrograph of the circuit.

exponentially, as

$$I(t) = I_0 e^{-\frac{t}{\tau}} \quad (8)$$

where  $I_0$  represents the initial fluorescence intensity at  $t = 0$ .  $\tau$  is the fluorescence lifetime and denotes the time duration required for the fluorescence to decay from the initial intensity  $I_0$  to  $I_0/e$ . To analyze the spectrum of the exponential decay curve of (8), its Fourier transform can be obtained as

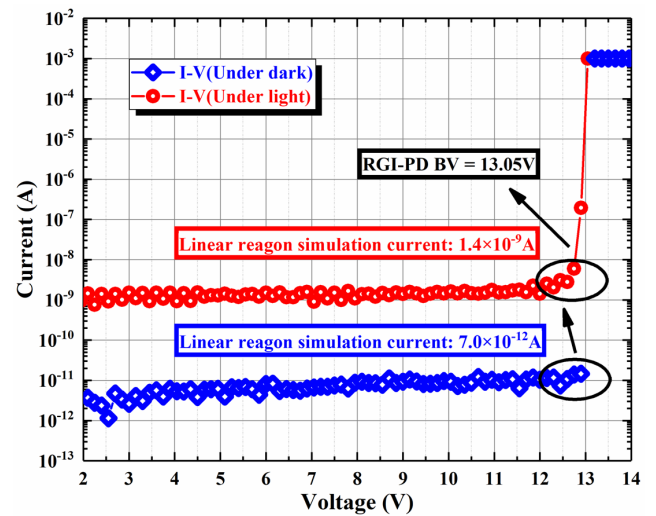
$$I(2\pi f) = I_0 \tau / (1 + j \cdot 2\pi f \cdot \tau). \quad (9)$$

The magnitude spectrum function of (9) can be obtained as

$$|I(2\pi f)| = I_0 \tau / \sqrt{1 + (2\pi f)^2 \tau^2}. \quad (10)$$

The spectral magnitude of the fluorescence decay curve decreases with increasing frequency, as derived from (10). The maximum magnitude occurs at  $f = 0$  Hz. The fluorescence lifetime of a rare earth fluorescent material, which contains europium ions ( $\text{Eu}^{3+}$ ), is approximately 2.5 ms at room temperature [5]. According to (10), the magnitude at  $f = 0$  Hz can be calculated as

$$|I(0)| = 2.5 I_0 / \sqrt{1 + 0\tau^2} = 2.5 I_0. \quad (11)$$

Fig. 12. Measurement results of the  $I$ - $V$  characteristics of the RGI-PD device.

Similarly, the magnitude at  $f = 1$  kHz can be calculated as

$$|I(2000\pi)| = I_0 \tau / \sqrt{1 + (2\pi f)^2 \tau^2} \approx I_0 / 2000\pi \ll 2.5 I_0. \quad (12)$$

The spectral magnitude at 1 kHz is much smaller than that at 0 Hz, suggesting negligible contribution from the frequency components beyond 1 kHz. Therefore, the TIA with a bandwidth larger than 1 kHz guarantees negligible fluorescence signal distortion.

Increasing the feedback resistor  $R_F$  can effectively reduce the power spectral density of the IRN current, as indicated by (3). However, this noise reduction comes at the cost of sacrificing the bandwidth. Since the bandwidth of TIA does not need to be too high and the weak fluorescence signal usually falls within the nanoampere range, a larger feedback resistor  $R_F$  is utilized. Hence, the  $R_F$  is 1 MΩ and the feedback compensation capacitor  $C_F$  is 24 pF. Consequently, the bandwidth of the circuit could be derived as follows, leading to a value of 6631.46 Hz:

$$f = 1 / (2\pi R_F C_F) = 6631.46 \text{ Hz}. \quad (13)$$

With this bandwidth range, the fluorescence signal can be received without distortion, thereby ensuring the integrity of

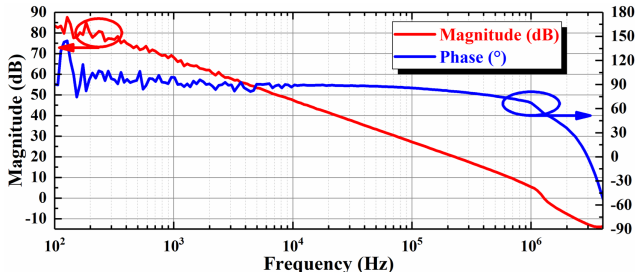


Fig. 13. Measurement results of the frequency response analysis of the feedforward amplifier.

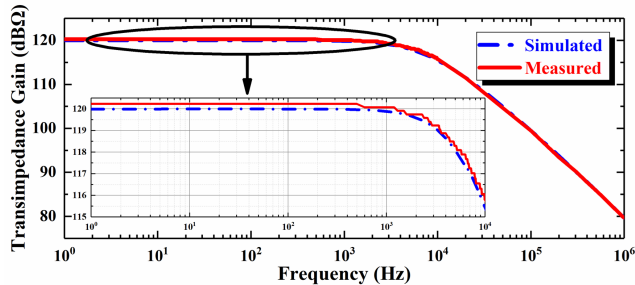


Fig. 14. Measurement results of the frequency response analysis of the TIA.

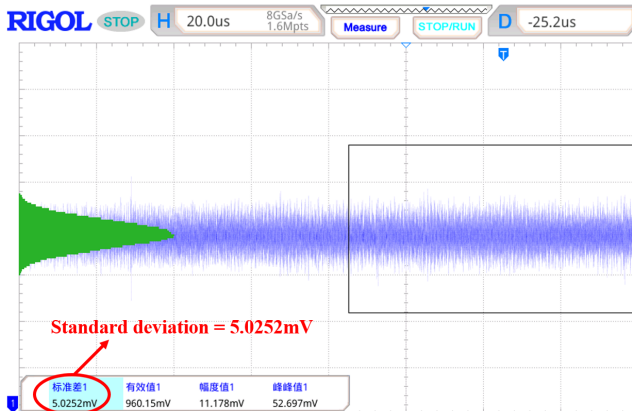


Fig. 15. Measured noise of the TIA.

the fluorescence signal readout. In this front-end design, the BGR circuit provides a highly robust reference voltage  $V_{\text{REF}}$  and a reference current  $I_{\text{REF}}$  for the feedforward amplifier. The reference current  $I_{\text{REF}}$  biases the feedforward amplifier to operate normally. The reference voltage  $V_{\text{REF}}$  is directly connected to the non-inverting input of the feedforward amplifier. This causes the anode voltage of the RGI-PD to be  $V_{\text{REF}}$ . By applying a bias voltage  $V_B$  to the cathode of the RGI-PD device, the photodiode can be reverse-biased and generate the photocurrent signal  $I_{\text{PD}}$ .

Our previous work [27] provides a detailed schematic circuit and working theory of the BGR voltage source. The feedforward amplifier, as the core module of the front-end circuit, directly determines their photoelectric conversion capability. For maximal input signal range and full output voltage swing, a feedforward amplifier with rail-to-rail functionality was selected for this design. The transistor-level circuit of the feedforward amplifier is shown in Fig. 10. The circuit topology adopts the transconductance equalization circuit, complementary input differential pair circuit, maximum current selection circuit, and floating class AB output stage used in the SUNY AT STONY BROOK UNIVERSITY [28]. To archive

rail-to-rail input capability, a complementary differential input pair consisting of transistors  $M_{15}-M_{18}$  was adopted in the input stage of the feedforward amplifier. As the hole mobility in pMOS transistors is smaller than the electron mobility in nMOS transistors, the pMOS transistor size needs to be approximately three times larger than the nMOS transistor size to achieve equal transconductance as per the parameters of the selected process for fabrication. This allows the complementary differential input pair to achieve linear response over the entire input voltage range, thus enabling rail-to-rail input capability. However, the transconductance of the input stage of the complementary differential pair varies with a common-mode input signal. This could be mitigated by adopting a transconductance equalization circuit ( $M_1-M_8$ ) and a maximum current selection circuit ( $M_{29}-M_{36}$ ). This approach enables the feedforward amplifier to maintain a relatively constant transconductance over the entire common-mode input voltage range with minimal relative error. To achieve rail-to-rail output swing, a Class AB configuration is employed as the output stage of the feedforward amplifier. Additionally, a floating complementary bias structure composed of two linear transconductance circuits is used to maintain a constant gate voltage for the output stage transistors of  $M_{57}$  and  $M_{58}$ . This not only enhances the feedforward amplifier's driving capability, but also reduces crossover distortion. Table II presents the design parameters and key size information of the feedforward amplifier.

#### IV. EXPERIMENTAL RESULTS AND DISCUSSIONS

The proposed front-end circuit of fluorescence optical temperature sensor with RGI-PD has been designed and fabricated using a  $0.18 \mu\text{m}$  BCD process. The layout and micrograph of the circuit are illustrated in Fig. 11. The chip has an effective area of  $606 \times 422 \mu\text{m}^2$ . The cathode of the RGI-PD device is connected externally to the bias voltage  $V_B$ , while a voltage source supplies the power of the BGR circuit and feedforward amplifier. The BGR circuit provides the reference voltage and current to the feedforward amplifier. The feedforward amplifier along with the on-chip feedback resistor  $R_F$  and compensation capacitor  $C_F$  forms a TIA.

The voltage-current characteristics of the RGI-PD device were measured using a Keysight power device analyzer B1505A. The measurement environment was categorized into two conditions dark and light. The  $I-V$  measurement results of the RGI-PD device are presented in Fig. 12. The avalanche  $\text{BV}$  ( $V_B$ ) of the device remained constant at  $13.05 \text{ V}$  and was unaffected by the light conditions. Under the dark condition, the current of the RGI-PD device in the linear region is measured to be  $7.0 \times 10^{-12} \text{ A}$ . When the avalanche response is triggered by the dark carriers, the current sharply surges to the milliampere level. With incident light on the photosensitive area of the device, several photo-generated electron-hole pairs are excited by the photons, leading to an increase in the current level to  $1.4 \times 10^{-9} \text{ A}$  in the linear region. The avalanche effect caused by the photons also instantaneously boosts the photocurrent to the milliampere level, reaching a saturation state. Comparing the simulation and measurement results, one can observe similarities in  $\text{BV}$ , despite slight differences due to the different illumination conditions. Hence, the measured results are in good agreement with the simulation results.

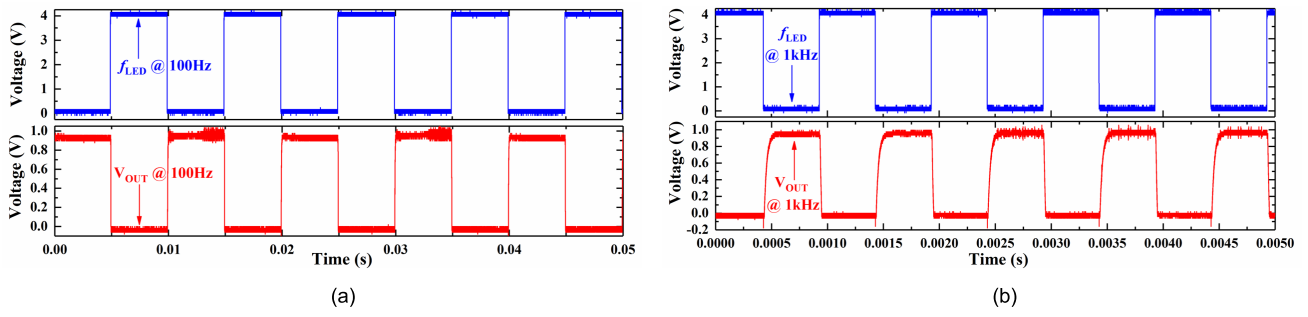


Fig. 16. Measurement results of frequency response for the optical sensor front-end circuit (a)  $f_{LED} = 100$  Hz and (b)  $f_{LED} = 3$  kHz.

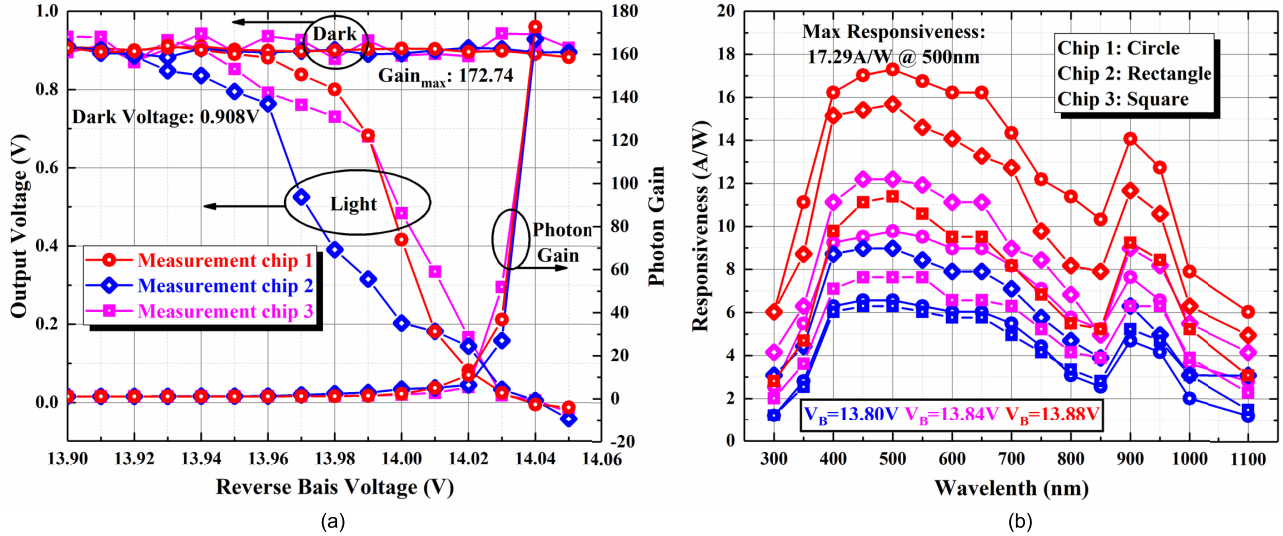


Fig. 17. Measurement results of the optical sensor front-end circuit. Output voltage with varying reverse bias voltage for three chips. (b) Spectral response for three chips.

The frequency response of the feedforward amplifier was measured by using the built-in function/arbitrary waveform generator of the Keysight Infinivision X series oscilloscope. To avoid any dc bias and isolate ac interference signals, the Picotest N2101A injection transformer was utilized. Additionally, a 1:1 passive probe was employed to reduce the influence of oscilloscope noise and switch noise, thus improving the SNR. Measured results are shown in Fig. 13. At a frequency of 100 Hz, the gain of the opamp is 83.46 dB; the phase margin is 54°; and the unit gain bandwidth is 1.28 MHz. To evaluate the TIA's frequency response, a 1 MΩ off-chip resistor is connected in series between the feedforward amplifier's inverting input and a signal generator. A RIGOL DG5352 arbitrary waveform generator produces a 1 V peak-to-peak ( $V_{PP}$ ) sinusoidal input voltage,  $V_{IN}$ . This configuration allows  $V_{IN}$ , in conjunction with the off-chip resistor, to generate a 1 μA peak-to-peak input current signal,  $I_{IN}$ . The RIGOL MSO5104 oscilloscope is used to display the output voltage  $V_{OUT}$ . Withholding the sinusoidal signal at 1  $V_{PP}$  and varying its frequency, the TIA's  $V_{OUT}$  is recorded and the transimpedance gain curve is obtained, as shown in Fig. 14. Measurements results show that the proposed TIA has a transimpedance gain of 120.23 dBΩ and a -3 dB bandwidth of 6.7 kHz. The noise bandwidth was extended to 0.95 MHz because the 40 dB attenuation (corresponding to 1% passband signal amplitude) occurs at this frequency. For noise measurements [29], we utilized a RIGOL MSO5104 oscilloscope to capture the output noise voltage of the proposed TIA. The standard deviation is 1.5025 mV.

without any input signals, as depicted in Fig. 15. To enhance the precision, the measured oscilloscope's inherent noise level of 2.4194 mV<sub>rms</sub> is deducted. Therefore, the IRN current of the TIA can be calculated as

$$I_{n,in} = \frac{2\sqrt{5.0252^2 - 2.4194^2}}{120.23\text{dB}} = 8.579 \text{ nA}_{\text{rms}}. \quad (14)$$

Hence, the average IRN current spectral density is given by

$$I_{n,in,\text{avg}} = I_{n,in} / \sqrt{\text{Noise(BW)}} = 8.798 \text{ pA}/\sqrt{\text{Hz}}. \quad (15)$$

To measure the transient response of the proposed fluorescence optical temperature sensor front-end circuit, it is necessary to construct an off-chip LED driving circuit, as shown in Fig. 9(a). By applying a square wave signal with 4 V amplitude and a specific frequency to the base of transistor S9014, the circuit is able to drive the LED operating at a fixed frequency. The selected LED produces a green light with a 500 nm wavelength. To determine the frequency response range of the proposed optical sensor front-end circuit, square wave signals with varying frequencies were applied to the input of the off-chip LED driving circuit. The resulting non-distorted output waveform was observed and recorded, as shown in Fig. 16. The output voltage ( $V_{OUT}$ ) of the optical sensor front-end circuit responded well to the LED driving signal ( $V_{LED}$ ) at low frequency, such as 100 Hz. As the frequency of the driving signal increases,  $V_{OUT}$  gradually distorts, such as 1 kHz. Nevertheless, it is enough for the detection of fluorescence decay signals.

**TABLE III**  
PERFORMANCE COMPARISON OF OUR WORK WITH OTHER REFERENCE

References	Ref. [8]	Ref. [12]	Ref. [15]	Ref. [16]	This work
Technology	350 nm CMOS	500 nm CMOS	180 nm CMOS	130 nm CMOS	180 nm BCD
Supply	3.3 V	5 V	1.8 V	1.2 V	3.3 V
Gain	131 dBΩ	130 dBΩ	79.4 dBΩ	98.6 dBΩ	120.23 dBΩ
Bandwidth	15 MHz	18 MHz	690 MHz	43.3 kHz	6.7 kHz
IRN	3 nA <sub>rms</sub>	4.1 nA <sub>rms</sub>	320 nA <sub>rms</sub>	1.89 nA <sub>rms</sub>	8.579 nA <sub>rms</sub>
Power dissipation	60 mW	7.5 mW	19.1 mW	2.16 mW	1.12 mW
Responsivity	0.9 A/W	0.23 A/W	0.25A/W	0.45 A/W	17.29 A/W
Chip area	2.16 mm <sup>2</sup>	4.4 mm <sup>2</sup>	0.519 mm <sup>2</sup>	2.2 mm <sup>2</sup>	0.25 mm <sup>2</sup>
FoM	4548.6	3706.6	4317.8	213.9	5798.1
PD type	Off-chip	On-chip	Off-chip	Off-chip	On-chip

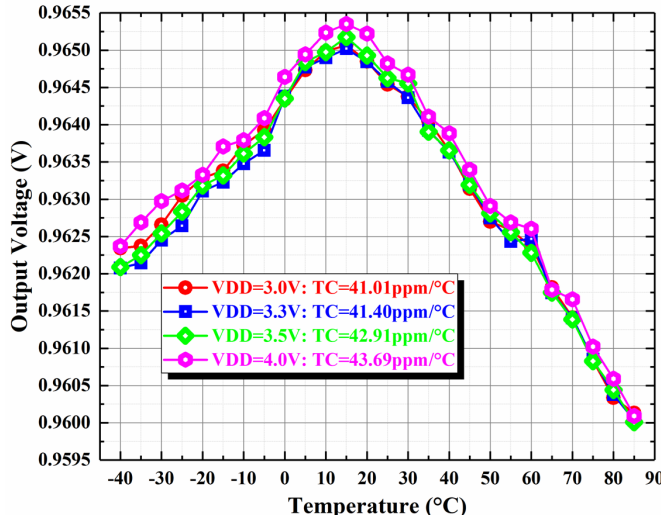


Fig. 18. TC measurement of the front-end circuit.

The spectral response of the proposed optical sensor front-end circuit, comprising an RGI-PD device and a TIA with BGR, was measured using a QE-IPCE-K6517B UV detector system. A xenon lamp is used as the light source, covering a wavelength range of 300 to 1100 nm with a resolution of 0.1 nm. The output light spot size was set to  $1 \times 1 \text{ mm}^2$ , and the intensity was 37.3 nW. Two groups of comparative experiments were carried out on the optical sensor front-end circuit. One is under the dark condition, the other is under the light condition. Fig. 17(a) shows the TIA output voltage variation with RGI-PD cathode voltage ( $V_B$ ) varying from 13.9 to 14.05 V for three front-end chips. Under the dark condition, it remains stable at 0.908 V, which is the output reference voltage of the BGR. Under the light conditions, it decreases as the reverse bias voltage  $V_B$  increases. When  $V_B$  approaches 14 V, the output voltage decreases sharply. Finally, when  $V_B$  increases to 14.04 V, the output voltage approaches zero. The photon gain curve, represented by the red line, is obtained by dividing the output voltage under light by the one under dark. When  $V_B$  is less than 14 V, the photon gain is expectedly small. When the RGI-PD device is under reverse bias and the reverse bias voltage  $V_B$  approaches 14 V, the photon gain will increase sharply at this point. This is because the bias voltage  $V_B$  is close to the avalanche breakdown threshold voltage of the front-end circuit, which is approximately equal to the sum of the avalanche BV of the RGI-PD device and the BGR voltage. The RGI-PD device transitions from the linear region to the avalanche multiplication region, resulting in a significant increase in photocurrent  $I_{PD}$ . With further increase in  $V_B$ , the photocurrent

$I_{PD}$  instantaneously surges to the milliampere level. From (7), it can be recollected that when the photocurrent  $I_{PD}$  increases significantly, the system output voltage drops to zero. These measurement results validate our theoretical analysis.

The output voltage  $V_{OUT}$  of the optical sensor front-end was recorded while varying the light source wavelength from 300 to 1100 nm, with a power supply voltage of 3.3 V and three different bias voltages  $V_B$ . According to (7), it can be observed that the photocurrent  $I_{PD}$  exhibits a negative linear correlation with output voltage  $V_{OUT}$ . This means higher spectral responsivity leads to a smaller  $V_{OUT}$ . Therefore, the photocurrent  $I_{PD}$  is obtained by solving (7). Furthermore, dividing  $I_{PD}$  by the optical power at each wavelength, results in the spectral response of the front-end circuit. Fig. 17(b) shows the spectral response variation with  $V_B$  varying from 13.8 to 13.88 V for three front-end chips. One can observe that the optimal spectral response range is between 400 and 700 nm. The maximum responsivity of 17.29 A/W is achieved at a wavelength of 500 nm under a  $V_B$  of 12.88 V.

Finally, high and low-temperature tests in the dark conditions were undertaken to analyze its temperature performance. The chip was placed in a constant temperature and humidity box. In the dark condition, the output voltage of the front end should be equal to the BGR voltage  $V_{REF}$ , which is independent of the temperature. The temperature is varied from  $-40^\circ\text{C}$  to  $85^\circ\text{C}$  and the power supply voltage  $VDD$  varies from 3 to 4 V in the measurement. The output voltage values of the chip were recorded at each temperature using a B2910BL precision source/measure unit. Fig. 18 shows the measurement results of the temperature coefficient (TC) of the front-end circuit. The circuit's TC reaches its optimal value of 41.01 ppm/ $^\circ\text{C}$  when  $VDD$  is set to 3 V. As  $VDD$  increases, the TC value also increases, reaching a value of 43.69 ppm/ $^\circ\text{C}$  at  $VDD = 4$  V. This can reflect the temperature effect on the front-end, mainly the BGR circuit. The measured TC is small enough to be a good temperature reference [30], [31]. The proposed front-end circuit operates at 3.3 V, with a static current of  $340 \mu\text{A}$ , resulting in a power consumption of 1.12 mW. Table III shows the performance comparison of the proposed front-end circuit with others' work. It is apparent that the proposed circuit achieves less power consumption, superior noise performance, and a higher TIA's gain. Due to the integration of the temperature sensor front-end circuit with the proposed RGI-PD in one chip, for the comparison in more complete dimensions, we introduce the PD responsivity and total chip area in the Figure of Merit (FoM) as below

$$\text{FoM} = \frac{\text{Gain}(\text{dB}\Omega) \cdot \text{BW}(\text{kHz}) \cdot R(\text{A/W})}{\text{IRN}(\text{nA}_\text{rms}) \cdot \text{Power}(\text{mW}) \cdot \text{Area}(\text{mm}^2)}. \quad (16)$$

In Table III, it is clearly seen that the FoM of the proposed front-end circuit is better than the other works. In short, this work exhibits several competing performances. Moreover, the proposed front-end circuit exhibits high robustness with respect to the temperature and voltage supply. These features make the front-end circuit suitable for fluorescent temperature measurement system applications.

## V. CONCLUSION

This article proposed an integrated front-end circuit for a fluorescent optical fiber temperature sensor with detection and amplification capabilities, designed and fabricated using a standard 0.18  $\mu\text{m}$  BCD process. The inverted pyramid hole profile in the RGI-PD focuses the electric field to suppress edge breakdown and enhance photodetection. While the TIA circuit transformed the photocurrent into measurable photovoltage output. Measurement results demonstrated that the RGI-PD device had an avalanche BV of 13.05 V and a peak responsivity of 17.29 A/W. Additionally, the TC of the front-end circuit was measured as 41.01 ppm/ $^{\circ}\text{C}$  in the temperature range from  $-40^{\circ}\text{C}$  to  $85^{\circ}\text{C}$ . In summary, silicon-based optical sensors have become the prevailing technology in optoelectronic integrated circuits, due to their potential for low-cost manufacturing and high-density integration. The proposed optical front-end with an on-chip integrated RGI-PD device is applicable to high-precision fluorescence fiber optic temperature sensing systems and can provide valuable references for fluorescence detection systems.

## REFERENCES

- [1] H. T. Lam, Y. Kostov, L. Tolosa, S. Falk, and G. Rao, "A high-resolution non-contact fluorescence-based temperature sensor for neonatal care," *Meas. Sci. Technol.*, vol. 23, no. 3, Feb. 2012, Art. no. 035104, doi: [10.1088/0957-0233/23/3/035104](https://doi.org/10.1088/0957-0233/23/3/035104).
- [2] M. Meribout, "Sensor systems for solar plant monitoring," *IEEE Trans. Instrum. Meas.*, vol. 72, 2023, Art. no. 9502016, doi: [10.1109/TIM.2022.3212990](https://doi.org/10.1109/TIM.2022.3212990).
- [3] W. Liu et al., "A reliable anti-interference probe based on fluorescence intensity ratio technique for cryogenic temperature detection," *J. Lightw. Technol.*, vol. 40, no. 21, pp. 7219–7225, Nov. 2022, doi: [10.1109/JLT.2022.3200387](https://doi.org/10.1109/JLT.2022.3200387).
- [4] D. E. Schwartz, E. Charbon, and K. L. Shepard, "A single-photon avalanche diode array for fluorescence lifetime imaging microscopy," *IEEE J. Solid-State Circuits*, vol. 43, no. 11, pp. 2546–2557, Nov. 2008, doi: [10.1109/JSSC.2008.2005818](https://doi.org/10.1109/JSSC.2008.2005818).
- [5] J. Yang, Y. Wang, X. Jin, Y. Peng, and J. Luo, "A novel high precision weighted integral ratio algorithm for fluorescent optical fiber temperature sensor," *Opt. Quantum Electron.*, vol. 54, p. 17, Nov. 2022, doi: [10.1007/s11082-021-03401-0](https://doi.org/10.1007/s11082-021-03401-0).
- [6] S. Ma et al., "Optical fiber sensors for high-temperature monitoring: A review," *Sensors*, vol. 22, no. 15, p. 5722, 2022, doi: [10.3390/s22155722](https://doi.org/10.3390/s22155722).
- [7] L. Hong and K. Sengupta, "Fully integrated optical spectrometer in visible and near-IR in CMOS," *IEEE Trans. Biomed. Circuits Syst.*, vol. 11, no. 6, pp. 1176–1191, Dec. 2017, doi: [10.1109/TBCAS.2017.2774603](https://doi.org/10.1109/TBCAS.2017.2774603).
- [8] S. Kurtti, A. Baharmast, J. Jansson, and J. Kostamovaara, "A low-noise and wide dynamic range 15 MHz CMOS receiver for pulsed time-of-flight laser ranging," *IEEE Sensors J.*, vol. 21, no. 20, pp. 22944–22955, Oct. 2021, doi: [10.1109/JSEN.2021.3105447](https://doi.org/10.1109/JSEN.2021.3105447).
- [9] V. Kumar, S. K. Raghuwanshi, and S. Kumar, "Advances in nanocomposite thin-film-based optical fiber sensors for environmental health monitoring—A review," *IEEE Sensors J.*, vol. 22, no. 15, pp. 14696–14707, Aug. 2022, doi: [10.1109/JSEN.2022.3185004](https://doi.org/10.1109/JSEN.2022.3185004).
- [10] B. Li et al., "Fluorescent optical fiber intensity ratio temperature sensor based on polymer matrix using down-conversion from ZnS: Cu," *IEEE Trans. Instrum. Meas.*, vol. 71, 2022, Art. no. 7006607, doi: [10.1109/TIM.2022.3198760](https://doi.org/10.1109/TIM.2022.3198760).
- [11] P. S. Pandey, S. K. Raghuwanshi, and S. Kumar, "Recent advances in two-dimensional materials-based Kretschmann configuration for SPR sensors: A review," *IEEE Sensors J.*, vol. 22, no. 2, pp. 1069–1080, Jan. 2022, doi: [10.1109/JSEN.2021.3133007](https://doi.org/10.1109/JSEN.2021.3133007).
- [12] Z.-K. Zhou, Y.-K. Wang, H.-G. Gong, Y. Shi, Z. Wang, and B. Zhang, "A fully-integrated optoelectronic detector with high gain bandwidth product," *IEEE Access*, vol. 7, pp. 53032–53039, 2019, doi: [10.1109/ACCESS.2019.2912639](https://doi.org/10.1109/ACCESS.2019.2912639).
- [13] D. Patel, A. Sharif-Bakhtiar, and T. C. Carusone, "A 112-Gb/s-8.2-dBm sensitivity 4-PAM linear TIA in 16-nm CMOS with co-packaged photodiodes," *IEEE J. Solid-State Circuits*, vol. 58, no. 3, pp. 771–784, Mar. 2023, doi: [10.1109/JSSC.2022.3218558](https://doi.org/10.1109/JSSC.2022.3218558).
- [14] C. Gasser, B. Goll, and H. Zimmermann, "Highly sensitive hybrid optical receiver with a compact 1.4 GHz linear transimpedance amplifier in 55 nm CMOS," *Opt. Eng.*, vol. 62, no. 9, Sep. 2023, Art. no. 095103, doi: [10.1117/1.OE.62.9.095103](https://doi.org/10.1117/1.OE.62.9.095103).
- [15] X. Li, H. Wang, J. Zhu, and C. P. Yue, "Dual-photodiode differential receivers achieving double photodetection area for gigabit-per-second optical wireless communication," *IEEE J. Solid-State Circuits*, vol. 58, no. 6, pp. 1681–1692, Jun. 2023, doi: [10.1109/JSSC.2023.3247950](https://doi.org/10.1109/JSSC.2023.3247950).
- [16] Y. He, J.-H. Kim, and S. M. Park, "A CMOS read-out IC for cyanobacteria detection with 40 nApp sensitivity and 45-dB dynamic range," *IEEE Sensors J.*, vol. 20, no. 8, pp. 4283–4289, Apr. 2020, doi: [10.1109/JSEN.2019.2962858](https://doi.org/10.1109/JSEN.2019.2962858).
- [17] A. Shadab, S. K. Raghuwanshi, and S. Kumar, "Advances in micro-fabricated fiber Bragg grating for detection of physical, chemical, and biological parameters—A review," *IEEE Sensors J.*, vol. 22, no. 16, pp. 15650–15660, Aug. 2022, doi: [10.1109/JSEN.2022.3188813](https://doi.org/10.1109/JSEN.2022.3188813).
- [18] H. Gu and L. Wang, "A high-detection-efficiency optoelectronic device for trace cadmium detection," *Sensors*, vol. 22, no. 15, p. 5630, 2022, doi: [10.3390/s22155630](https://doi.org/10.3390/s22155630).
- [19] J. Musayev, Y. Adlgüzel, H. Külah, S. Eminoglu, and T. Akln, "Label-free DNA detection using a charge sensitive CMOS microarray sensor chip," *IEEE Sensors J.*, vol. 14, no. 5, pp. 1608–1616, May 2014, doi: [10.1109/JSEN.2014.2301693](https://doi.org/10.1109/JSEN.2014.2301693).
- [20] J. Guo, J. Zhang, S. Thomas, and S. Sonkusale, "CMOS fluorometer for oxygen sensing," *IEEE Sensors J.*, vol. 12, no. 7, pp. 2506–2507, Jul. 2012, doi: [10.1109/JSEN.2012.2194280](https://doi.org/10.1109/JSEN.2012.2194280).
- [21] B. R. Rae et al., "A vertically integrated CMOS microsystem for time-resolved fluorescence analysis," *IEEE Trans. Biomed. Circuits Syst.*, vol. 4, no. 6, pp. 437–444, Dec. 2010, doi: [10.1109/TBCAS.2010.2077290](https://doi.org/10.1109/TBCAS.2010.2077290).
- [22] D. Bronzi et al., "100 000 Frames/s 64×32 single-photon detector array for 2-D imaging and 3-D ranging," *IEEE J. Sel. Topics Quantum Electron.*, vol. 20, no. 6, pp. 355–364, Nov. 2014, doi: [10.1109/JSTQE.2014.2341562](https://doi.org/10.1109/JSTQE.2014.2341562).
- [23] A. Manickam et al., "A fully integrated CMOS fluorescence biochip for DNA and RNA testing," *IEEE J. Solid-State Circuits*, vol. 52, no. 11, pp. 2857–2870, Nov. 2017, doi: [10.1109/JSSC.2017.2754363](https://doi.org/10.1109/JSSC.2017.2754363).
- [24] L. Hong, H. Li, H. Yang, and K. Sengupta, "Fully integrated fluorescence biosensors on-chip employing multi-functional nanoplasmonic optical structures in CMOS," *IEEE J. Solid-State Circuits*, vol. 52, no. 9, pp. 2388–2406, Sep. 2017, doi: [10.1109/JSSC.2017.2712612](https://doi.org/10.1109/JSSC.2017.2712612).
- [25] J. Choi et al., "Fully integrated time-gated 3D fluorescence imager for deep neural imaging," *IEEE Trans. Biomed. Circuits Syst.*, vol. 14, no. 4, pp. 636–645, Aug. 2020, doi: [10.1109/TBCAS.2020.3008513](https://doi.org/10.1109/TBCAS.2020.3008513).
- [26] H. Jiang and P. K. L. Yu, "Equivalent circuit analysis of harmonic distortions in photodiode," *IEEE Photon. Technol. Lett.*, vol. 10, no. 11, pp. 1608–1610, Nov. 1998, doi: [10.1109/68.726765](https://doi.org/10.1109/68.726765).
- [27] X. Jin and B. Xiong, "Low-voltage bandgap reference based on deep submicron technology," in *Proc. 7th Int. Conf. Inf. Sci. Control Eng. (ICISCE)*, Changsha, China, Dec. 2020, pp. 1923–1927, doi: [10.1109/ICISCE50968.2020.00378](https://doi.org/10.1109/ICISCE50968.2020.00378).
- [28] C. H. Lin, M. Ismail, and T. Pimenta, "Robust design of LV/LP low-distortion CMOS rail-to-rail input stages," *Analog Integr. Circuits Signal Process.*, vol. 21, pp. 153–162, Nov. 1999, doi: [10.1023/A:1008377925289](https://doi.org/10.1023/A:1008377925289).
- [29] J.-E. Joo, M.-J. Lee, and S. M. Park, "A CMOS fully differential optoelectronic receiver for short-range LiDAR sensors," *IEEE Sensors J.*, vol. 23, no. 5, pp. 4930–4939, Mar. 2023, doi: [10.1109/JSEN.2023.3236678](https://doi.org/10.1109/JSEN.2023.3236678).
- [30] O. Bass, A. Feldman, and J. Shor, "A resistor-less nW-level bandgap reference with fine-grained voltage and temperature coefficient trims," *IEEE Open J. Circuits Syst.*, vol. 3, pp. 192–198, 2022, doi: [10.1109/OJCAS.2022.3206326](https://doi.org/10.1109/OJCAS.2022.3206326).
- [31] C. Yu and L. Siek, "An area-efficient current-mode bandgap reference with intrinsic robust start-up behavior," *IEEE Trans. Circuits Syst. II, Exp. Briefs*, vol. 62, no. 10, pp. 937–941, Oct. 2015, doi: [10.1109/TCSII.2015.2458044](https://doi.org/10.1109/TCSII.2015.2458044).